Towards optical measurements of membrane potential values in *Bacillus subtilis* using fluorescence lifetime

Debjit Roy[1], Xavier Michalet*[2,5], Evan W. Miller[3], Shimon Weiss*[1,2,4,5,6]

[1]UCLA-DOE Institute for Genomics and Proteomics, Department of Biological Chemistry, University of California at Los Angeles, Los Angeles, CA 90095, USA, [2]Department of Chemistry and Biochemistry, University of California at Los Angeles, Los Angeles, CA 90095, USA, [3]Departments of Chemistry, Molecular and Cell Biology, Helen Wills Neuroscience Institute, University of California at Berkeley, CA 94720, USA, [4]Department of Physiology, University of California at Los Angeles, Los Angeles, CA 90095, USA, [5]California Nano Systems Institute, University of California at Los Angeles, Los Angeles, CA 90095, USA, [6]Department of Physics, Institute for Nanotechnology and Advanced Materials, Bar-Ilan University, Ramat-Gan 52900, Israel.

KEYWORDS Membrane Potential, Bacterial Electrophysiology, VoltageFluor, Fluorescence Lifetime Imaging Microscopy, Phasor Analysis.

ABSTRACT: Membrane potential (MP) changes can provide a simple readout of bacterial functional and metabolic state or stress levels. While several optical methods exist for measuring fast changes in MP in excitable cells, there is a dearth of such methods for absolute and precise measurements of steady-state membrane potentials (MPs) in bacterial cells. Conventional electrode-based methods for the measurement of MP are not suitable for calibrating optical methods in small bacterial cells. While optical measurement based on Nernstian indicators have been successfully used, they do not provide absolute or precise quantification of MP or its changes. We present a novel, calibrated MP recording approach to address this gap. Our method is based on (i) a unique VoltageFluor (VF) optical transducer, whose fluorescence lifetime varies as a function of MP via photoinduced electron transfer (PeT) and (ii) a quantitative phasor-FLIM analysis for high-throughput readout. This method allows MP changes to be easily recorded, quantified and visualized. Using our preliminary *Bacillus subtilis*-specific MP versus VF lifetime calibration, we estimated the MP for unperturbed *B. subtilis* cells to be -65 mV and that for chemically depolarized cells as -14 mV. Our work paves the way for deeper insights into bacterial electrophysiology and bioelectricity research.

1. Introduction

Cellular communication, pattern formation and behavior are governed not only by chemical cues (e.g., chemo-attractants, ion gradients, protein and RNA levels), but also by membrane electrical potentials.[3] The term bioelectricity is used to describe phenomena including changes in membrane potential (MP) that mediate and regulate electrical signaling between neighboring cells in a tissue or in a biofilm.[4] The membrane potential is defined as the electric potential difference across the membrane lipid bilayer and is maintained by the careful balance between the diffusion pressure created by ionic concentration gradient across the membrane and electrical forces arising from the separation of charges and the selective permeability of the membrane to certain ions. Additionally, charged/zwitterionic lipids, lipid-water dipole alignment, and fixed intracellular charges (DNA, RNA, ribosomes, and proteins) also contribute to the MP.[4]

The MP is an intrinsic characteristic of each cell type[5] which the cell tries to maintain to achieve homeostasis. Changes in MP is a mere reflection of changes in the cell's functional state, often trigger reflex responses due to external stimuli or follow downstream signaling pathways in various physiological processes such as cellular proliferation and differentiation.[6] MP changes drive various essential bacterial activity such as energy generation,[7] nutrient uptake and transport,[8] cell division,[9] metabolism,[10] osmoregulation,[11] mechano-sensation,[12] motility[13] and antibiotic resistance.[14] Intercellular communication and co-ordination between microbial cells during metabolism and stress response are accompanied, and possibly mediated by, dynamic MP changes followed by ion translocation (electro-chemical communication). Recent studies have shown that MP changes mediate cell-cell signaling in *Bacillus subtilis* (*B. subtilis*) bacterial communities,[15] coordinate metabolic oscillations radially within biofilms, broadcasting metabolic status amongst cells located within different parts of biofilms,[16] and enable dormant spores to integrate environmental signals.[17] In summary, the role of membrane potential in all aspects of bacterial physiology cannot be overemphasized and calls for robust and accurate means of quantifying it.

2. Optical Estimation of Resting Membrane Potential: problem and potential solution

However, calibrated measurements of absolute MPs and their changes are challenging. Past electrophysiological studies have mainly focused on specialized excitable mammalian cells (neurons, cardiomyocytes, muscle cells, and some secretory cells) and has led to the development of a fundamental framework and models for understanding bioelectricity. Slow changes in MP are common to most tissues

and bacterial cells, in contrast to action potentials (APs), *i.e.* fast MP changes, which are limited to specialized excitable cells. However, tools to *quantitatively* measure slow changes in MP trail behind tools used to simply detect APs.[18-21] In mammalian cells, electrode-based methods (patch-clamp or micro-electrode arrays) are considered the gold-standard for precise measurements of APs and MPs.[18-22] These techniques are sensitive, provide sub-ms temporal resolution, but have limited throughput and spatial resolution. Direct electrical potential measurements using microelectrodes has been achieved on artificially enlarged (genetically /pharmacologically) *E. coli* cells.[23] However, electrode-based tools are not suitably implementable for small sized bacterial cells. Alternatively, bacterial MP measurements resorted on the use of small molecule Nernstian indicators that exhibits MP change induced reversible accumulation-redistribution and monitored by radioactivity ($TPMP^+$, TPP^+)[24] or fluorescence (ThT, TMRM, Rh123) measurements.[25] Fluorescent Nernstian indicators have been until recently the main tool for studying bacterial membrane potential, as they allow live recording and long term studies of single cells or biofilms. These are in general cationic, membrane-permeable dyes, with a low membrane binding affinity. The equilibrium concentrations of such an indicator on both sides of the membrane are related to the value of the MP (noted V_m) by the Nernst equation:

$$V_m = \frac{k_B T}{Ze} \ln \frac{[X]_{out}}{[X]_{in}} \quad (1)$$

where Ze is the electric charge of indicator X, k_B is the Boltzmann constant, T the temperature and $[X]_{out/in}$ the outer/inner indicator concentrations, respectively. Assuming a linear dependence of fluorescence intensity with concentration, MP changes therefore translate into measurable logarithmic changes in the ratio of extracellular to cytoplasmic radioactivity or fluorescence intensities.

Fluorescent Nernstian indicators have been employed to measure bacterial MP, providing insight into electrical spiking in *E. coli*,[26] metabolic oscillations in *B. subtilis* biofilms,[15] external electrical stimuli induced bacterial MP fluctuations,[27] and values of resting MPs ranging from -140 mV to -75 mV.[23,28-30]

However, problems exist for Nernstian indicators. They lack fine sensitivity to small MP changes. Their temporal response is slow (seconds to minutes)[27,31] due to the diffusion-driven equilibration of the indicator. At high indicator concentration (>100 μM), cellular MP is likely perturbed,[32] and even low concentrations (>10 μM) of dye substantially slow the elongation rate of *B. subtilis* and *E. coli*.[33]

Like all indirect measurements, optical (or radiolabel-based) recordings of MP changes require additional calibration for absolute quantification. However, these measurements are often subjected to confounding effects due to variations in probe concentration, non-uniform microenvironment, probe loading efficiency, variable illumination intensity or background, and photobleaching. Careful control experiments are needed to minimize artifacts due to these variations. In particular, it is very hard to measure small MP changes using Nernstian indicators. For these reasons, better tools are desirable for studying bacterial bioelectricity in real-time, with appropriate spatial and temporal resolutions, and voltage sensitivity.

Another approach to MP measurement in bacteria is the use of genetically engineered voltage indicators (GEVIs) such as PROPS.[26,34,35] This powerful technique requires modifying the cell's genome, making it inappropriate for wild type cell studies, and using an inducer to control expression of the fluorescent GEVI, adding to the uncertainty and complexity of the measurements.

To address these limitations, we investigated the use of VoltageFluor dye VF2.1.Cl, a lipophilic dye characterized by a membrane potential-dependent fluorescence lifetime, which has been extensively characterized in eukaryotic cells.[36-39]

Fluorescence lifetime imaging microscopy (FLIM) is a powerful tool to monitor the nanoscale environment of biomolecules. The fluorescence lifetime τ is an intrinsic molecular property of a fluorophore and is only sensitive to alterations in intramolecular structure (conformational changes) and intermolecular interaction with its local electronic microenvironment. The measured fluorescence lifetime (but not its precision) is independent from the recorded fluorescence intensity and to a large extent from fluorophore concentration, simplifying calibration and reproducibility.[40] τ is an excellent indicator for local changes in temperature, polarity, viscosity, pH, ionic strength etc. Spatiotemporal mapping of these properties could be acquired via FLIM.[41-43] Quantification of MPs by measurement of the fluorescence lifetime of voltage sensitive dyes (VSDs) is therefore an attractive alternative to current approaches.

We used *B. subtilis*, a rod-shaped, Gram-positive model bacterium (i.e., with a single membrane), and VoltageFluor (VF) dyes as a proof-of-concept testbed. Because patch-clamp is not an option in bacteria, we controlled the MP by addition of chemicals extracellularly and limited ourselves to equilibrium measurements of VF's fluorescence lifetime after a fixed incubation time. Our results are organized as follows. In section 3, the photophysical characterization of VF dyes in solution and in live *B. subtilis* membrane is reported. We discuss the effect of MP-induced changes on the photoinduced electron transfer (PeT) kinetic rate affecting the fluorescence lifetime of the VF indicators using a simplified model introduced by Li.[44] In section 4, we briefly describe the phasor analysis of fluorescence lifetime used in our experiments and compare it with the conventional non-linear least-square fitting (NLSF) approach. Section 5 presents our experiments towards calibration of MP via phasor-FLIM measurements. We report average VF2.1Cl fluorescence lifetime changes observed at the single-cell level, and interpret these changes within the previously described framework. *B. subtilis*'s MP estimated in unperturbed and depolarizing chemical conditions are reported in section 6. We further probe the effect of medium osmolality on MP in section 7. Color-coded fluorescence lifetime maps visualizing MP changes are discussed in section 8, before a summary and critical discussion of our results are presented in section 9. Materials and methods are briefly described in section 10.

3. Photophysical characterization of VoltageFluor lifetime in solution and in the membrane of *B. subtilis*

In this work, we used two dyes to measure bacterial MP (Figure 1a): (i) VF2.1.Cl, a voltage-sensitive fluorophore,[36,37,45] and (ii) VF2.0.Cl, an isostructural control dye which is not voltage sensitive.

Both VF2.1.Cl (voltage-sensitive) and VF2.0.Cl (insensitive) localize to the plasma membrane of mammalian cells. VF2.1.Cl displays voltage- and electric field-dependent fluorescence[46] arising from a photoinduced electron transfer (PeT) from the electron rich aniline into the excited state of the fluorescein fluorophore (Fig. 1a).[36,37,45] At hyperpolarized potentials (negative inside), the rate of PeT is accelerated by alignment with the electric field of the membrane,

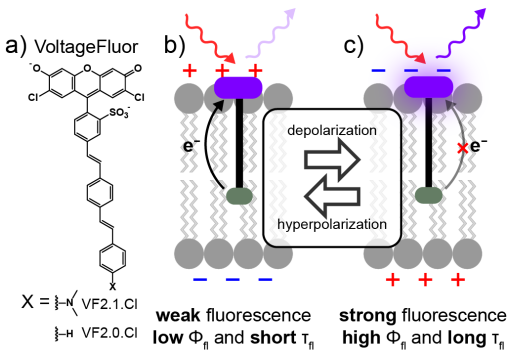

Figure 1: Voltage-sensitive fluorophore VF2.1.Cl. VF2.1.Cl senses MP via photoinduced-electron transfer. In mammalian cells, in the -80 mV to +80 mV range of transmembrane voltage, it exhibits a relative fluorescence intensity (ΔF/F) change of ~27% per 100 mV and $\Delta\tau_{avg}$ ~3 ps/mV. a) When the membrane gets hyperpolarized, PeT is increased and fluorescence is quenched, b) When the membrane gets depolarized, PeT is reduced and fluorescence enhanced c) Chemical molecular structure of VF2.1.Cl (adapted from [1]).

making the dye dim (Fig. 1b). At depolarized potentials (positive inside), the rate of PeT is slowed by opposing electric field, making the dye bright (Fig. 1c). VF2.0.Cl shows no voltage-dependent fluorescence, in either intensity or lifetime modes.[38,47]

The mechanism of voltage sensing relies on dependence of the sensor's intrinsic PeT process on the local electric field *E*. PeT is a non-radiative relaxation pathway from the dye's first excited state S_1 to a charge-separated state S_2, which competes with radiative decay (characterized by fluorescence rate k_f) and other non-radiative processes (rate k_{nr}), as discussed in Supplementary Note 5 and illustrated in the Jablonski diagram shown in Supplementary Fig. S12. In the absence of PeT, a dye's fluorescence is normally characterized by a mono-exponential relaxation down to the ground state S_0 with rate $k_{10} = k_f + k_{nr}$ equal to the inverse of the measured fluorescence lifetime. This behavior was observed by the Miller group for VF2.0.Cl, which did not show voltage-dependent fluorescence intensity, in mammalian cells [38,47].

In the presence of PeT, hyperpolarized membranes (membranes with more negative membrane potential difference than the resting membrane potential) resulted in enhanced PeT, which led to increased nonradiative relaxation from the dye's excited state S_1 to the charge-separated state S_2 (rate $k_{12} = k_{PeT}$), followed by relaxation to the ground state S_0 (with rate k_{20}), resulting in an overall shorter average lifetime and dimmer fluorescence (Fig. 1a). Inversely, depolarized membranes resulted in reduced PeT and longer lifetime, *i.e.* brighter emission (Fig. 1b).[38,39,47-50]

Using the 3-state model described in Supplementary Note 5, one obtains the following result for the amplitude-averaged lifetime $\langle\tau\rangle_a$ (supplementary Eq. S11) and quantum yield Y_f (supplementary Eq. S10):

$$\langle\tau\rangle_a = \frac{Y_f}{k_f} \sim k_{10}^{-1}\left(1+\frac{k_{12}}{k_{10}}\right)^{-1}, \qquad (2)$$

where the membrane potential (V_m) dependence of $\langle\tau\rangle_a$ is encompassed in the electric field *E*-dependence of k_{12} via $V_m = E/d$, where *d* is the membrane thickness (supplementary Eqs. S7-S8). This dependence can be used to measure the membrane potential, after calibration of the VF's response to a series of externally applied membrane potentials.[38,51] The voltage sensitivity of various VF dyes has been previously characterized in cultured cells, dissociated mammalian neurons, and *ex vivo* leech ganglia under patch-clamp, which allowed precise control of the membrane potential.[37,38,47] Woodford *et al.* observed various types of dependence of the relative intensity change $\Delta F/F = \Delta Y/Y$ on V_m for a variety of VF dyes. In particular, VF2.1.Cl exhibited a linear dependence of $\Delta F/F$ on V_m in the ±80 mV range in HEK cells incubated in HBSS buffer.

These characteristics made VF2.1.Cl an ideal VF dye to test for bacterial membrane potential measurements. We chose *B. subtilis* as a model Gram-positive (single membrane) bacterial species, as it has been extensively characterized in the literature and is non-pathological.

We first compared the fluorescence lifetime of both VF2.1.Cl and VF2.0.Cl in solution and in bacterial membranes. In solution, VF2.1.Cl exhibited a faster fluorescence decay than VF2.0.Cl. due to the existence of an intrinsic PeT channel, absent in VF2.0.Cl (Supplementary Fig. 1). Specifically, VF2.0.Cl exhibited a single-exponential decay ($\langle\tau\rangle_{2.0,DMSO}$ = 3.21 ns), whereas VF2.1.Cl was characterized by a clear bi-exponential decay (τ_1 = 2.73 ns, τ_2 = 0.66 ns; $\langle\tau\rangle_{2.1,DMSO}$ = 1.44 ns) as obtained by NLSF analysis (Supplementary Table 2).

The membrane of *B. subtilis* was readily stained with both dyes (see Supplementary Note 1 for bacteria culture, growth and membrane staining protocols). The fluorescence signal appears limited to the membrane based on intensity profile analysis (Fig. 2 and Supplementary Note 6). The amplitude-averaged fluorescence lifetime of VF2.0.Cl in the membrane of *B. subtilis* was $\langle\tau\rangle_{2.0,mb}$ = 2.59 ns, while that of VF2.1.Cl was $\langle\tau\rangle_{2.1,mb}$ = 0.74 ns (τ_1 = 1.87 ns, τ_2 = 0.32 ns) (Supplementary Table 2). Interestingly, both decays exhibited two exponential components, including that of VF2.0.Cl. For VF2.1.Cl, the reduction of the average lifetime is related to the different environments of the VF and the presence of the transmembrane electric field associated with the membrane, as studied next.

4. Fluorescence lifetime analysis: nonlinear least-square fitting versus phasor approach

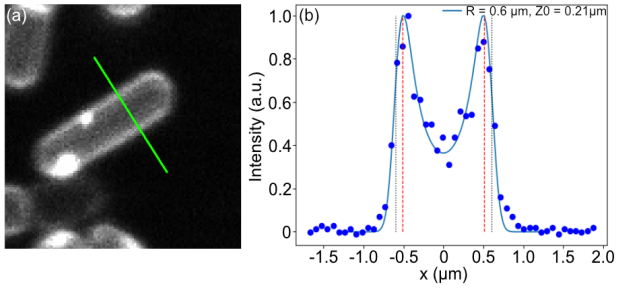

Figure 2: *B. subtilis* membrane staining with VF2.1.Cl. (a) Confocal image (72 nm/pixel) of an isolated bacterium. The corresponding intensity profile along the green segment is shown in b. Green bar indicates 1 µm. (b) Dots: intensity profile along the segment shown in a. The blue line corresponds to expected signal from a cylindrical fluorescent object with radius $R = 0.6$ µm (grey vertical line) and focus $z_0 = 210$ nm above the midplane. The apparent radius (red vertical line) is 0.51 µm.

Conventionally fluorescence lifetime determinations were performed by TSCPC FLIM followed by nonlinear least-square fitting (NLSF) of the recorded photon arrival time histogram. This is computationally expensive and requires high photon counts/good signal-to-noise ratio (SNR), especially for bi-exponential decays.[52,53] We therefore turned to phasor analysis.[54-65] Phasor analysis can be as quantitative as NLSF for bi-exponential decays when individual lifetime components are known or can be determined independently.[62,65,66] We compared the lifetime of VF2.1.Cl in *B. subtilis* determined by NLSF (741 ± 62 ps, Fig. 3a) and by phasor analysis (778 ± 38 ps, Fig. 3b). The values are in good agreement, the difference of 37 ps being due to different approximations used in both methods. Based on this agreement, we decided to use the phasor analysis approach in the remainder of this study, due to its speed and better reliability at low signal-to-noise ratio.[54-60]

5. Single cell membrane potential calibration of *B. subtilis* via phasor-FLIM measurements

The electric field across the membrane depends on local charge densities on both side of the membrane (whose possible non-homogeneity along the cell periphery is neglected in this work). This local density is connected by a boundary layer to the internal or external bulk ion concentrations, respectively, and can be described by various models, ranging from the simple Gouy-Chapman double-layer model[67] to more sophisticated ones solving the Poisson-Boltzmann equation (e.g. [68-70]). The important result of this type of analysis is that, far away from the membrane, the bulk ion concentrations can be considered constant and, at equilibrium, can be computed using the Donnan model[71] or, when taking the permeabilities p_i of the different ions through the membrane into account, the Goldman-Hodgkin-Katz (GHK) model:[4,67]

$$V_m = \frac{k_B T}{e} \ln \frac{p_{K^+}\left[K^+\right]_{out} + p_{Na^+}\left[Na^+\right]_{out} + p_{Cl^-}\left[Cl^-\right]_{in}}{p_{K^+}\left[K^+\right]_{in} + p_{Na^+}\left[Na^+\right]_{in} + p_{Cl^-}\left[Cl^-\right]_{out}} \quad (3)$$

where index *in* (resp. *out*) indicate concentration inside (resp. outside) the cell. Of the 3 monovalent ions (multivalent ions being less permeable are typically neglected) contributing most to the membrane potential (K^+, Na^+ and Cl^-), the first one is the most membrane permeable, leading to a GHK solution which is effectively well approximated by the Nernst potential of K^+ (Eq. (1)):

$$V_m \sim \frac{k_B T}{e} \ln \frac{\left[K^+\right]_{out}}{\left[K^+\right]_{in}} \quad (4)$$

Thus, if $[K^+]_{in}$ is known for a given external medium composition (with a specific $[K^+]_{out}$), the membrane potential can be computed using Eq. (4).

This estimated membrane potential is however not exactly the potential drop across the membrane, as there is a gradient of electrostatic potential in the vicinity of the membrane due to the presence of a gradient of ion concentrations, reducing the effective membrane potential drop to V_{mb}, as discussed in Supplementary Note 7. In most practical cases, the resulting electric field to which the dye is exposed, $E = V_{mb}/d$ is only slightly smaller (by 1-3%) than that estimated from the Nernst potential V_m (Eq. (4)), justifying neglecting this difference (see Supplementary Note 7 for details). Note that this estimate ignores the possible contribution of charged species residing within the external bacterial wall to the electrostatic potential, a point which will be discussed in the last section.

Patch clamp electrophysiology is impractical for controlling the MP of *B. subtilis*. Therefore, we needed another method to set the MP for a calibration. Since the MP stems from the unequal distribution of ions and charged species across the

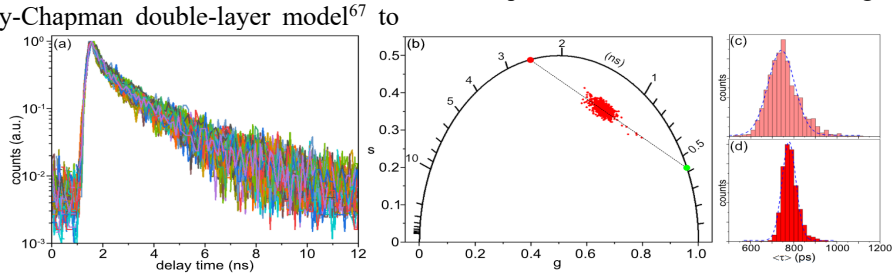

Figure 3: (a) 100 representative single-cell fluorescence decays for a population of *B. subtilis* cells stained with VF2.1.Cl (suspended in MSgg medium). Their fit with two-exponential decay model yields time constants $\tau_1 = 1.87 \pm 0.16$ ns and $\tau_2 = 0.32 \pm 0.05$ ns. (b) Corresponding phasor plot, with the single-exponential references (green and red dots on the UC, $\tau_1 = 2.51$ ns, $\tau_2 = 0.44$ ns) and the segment connecting them (dashed line). (c) amplitude-averaged lifetime <τ> histogram obtained via single- cell NLSF analysis (<τ> = 741 ± 62 ps) and (d) amplitude-averaged lifetime <τ> histogram obtained by single-cell phasor analysis (<τ> = 778 ± 32 ps). The two-sample t-test with Welch correction for unequal variance indicates a small but significant difference between the two distributions, which are attributable to small systematic differences resulting from different reference choices in NLSF and phasor analysis.

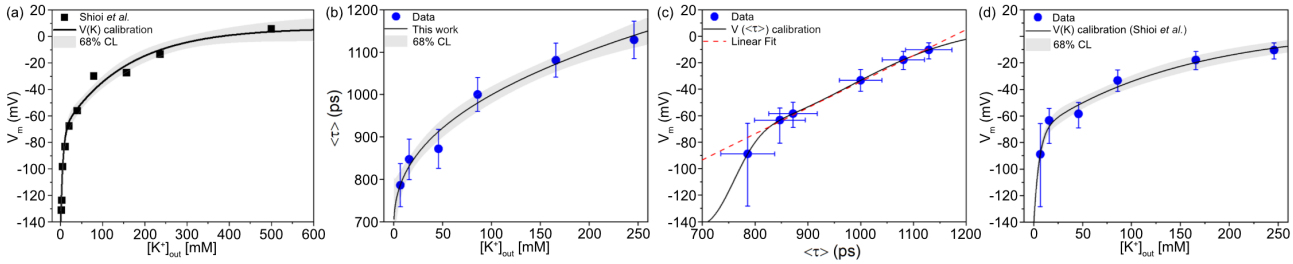

Figure 4: Calibration of the response of VF2.1.Cl to *B. subtilis* membrane potential changes. (a) *B. subtilis* membrane potential as function of external K^+ concentration measured with radioactive Nernstian probes in the presence of 10 µM valinomycin (adapted from Fig. 3 in ref. [2]). The line is a bi-exponential fit $V_m([K^+]_{out})$ to the data. (b) Measured averaged fluorescence lifetime <τ> of VF2.1.Cl in the membrane of *B. subtilis* as a function of external K^+ concentration measured in similar conditions as in (a) (medium osmolality ~650 mOsm/L). The line is a power law fit with offset <τ>($[K^+]_{out}$) to the data. (c) V_m *vs* <τ> calibration curve obtained by combining the two fitted relations shown in (a) & (b). The horizontal error bars indicate the standard deviation of the data used for calibration (as shown in b), while the vertical error bars represent the corresponding uncertainty in the membrane potential. The red dashed line corresponds to a linear fit of the data with slope 0.2 mV/ps. (d) V_m values obtained for the $[K^+]_{out}$ used in the calibration series using the $V_m([K^+]_{out})$ obtained in (a). The error bar was computed as in (c).

membrane (mainly K^+, as discussed previously), one way to modulate the MP is to artificially change ionic (K^+) concentration gradients across the membrane in conjunction with an ionophore. Ionophores, a class of physiologically active compounds[72-74] that facilitate selective ion transport across cell membranes (bypassing normal ion channels or transporters), can for instance be used to increase the membrane permeability for specific ions. and alter intracellular ionic compositions and ionic concentration gradients across the cell membranes. Here, we used valinomycin, a mobile carrier ionophore, known for selective translocation of K^+ across biological and synthetic membranes down the electrochemical potential gradient.[73,75-80] Valinomycin treatment effectively enhances the K^+ permeability through the cell membrane, making it impossible for the cell to effectively maintain its resting potential.[73,76-80] The accepted mechanism of K^+ transport by valinomycin involves binding to K^+ on one side of the membrane, dissolution into the membrane lipid bilayer, followed by transport and release of K^+ on the other side of the membrane.[76-78] The increased permeability of K^+, coupled with changing $[K^+]_{out}$ into the cell unsettles the existing K^+ concentration gradient, which is partially counterbalanced by the cell, but leads eventually to an altered $[K^+]_{in}/[K^+]_{out}$ ratio that differs from the original one, resulting in a different membrane potential.

We used a previously established V_m *vs* $[K^+]_{out}$ calibration curve measured in *B. subtilis* using Nernstian radiolabels ([^{3}H]triphenylmethylphosphonium bromide, $^3TPMP^+$) in the presence of valinomycin and varying external concentrations of K^+.[2] By measuring the inside and outside bulk concentrations of the indicator at equilibrium, $[^3TPMP^+]_{in}$ and $[^3TPMP^+]_{out}$, Shioi *et al.* were able to correlate $[K^+]_{out}$ and the membrane potential V_m computed with Eq. (1) for the indicator. Their data, obtained at variable $[K^+]_{out}$ but constant external osmolality, are reproduced in Fig. 4a.

We recorded the fluorescence lifetime of VF2.1.Cl at different $[K^+]_{out}$ in the presence of valinomycin (Fig. 4b), exactly reproducing the previous calibration conditions.[2] Briefly, *B. subtilis* cells in the mid-exponential phase were treated with 25 µM valinomycin and supplemented with various concentrations of KCl (1 to 240 mM) . To maintain constant medium osmolality, NaCl was added to keep the total cation concentration equal to 240 mM (medium osmolality ~650 mOsm/L). We then constructed a VF2.1.Cl lifetime *vs* V_m calibration curve by combining the previously obtained V_m *vs* $[K^+]_{out}$ data[2] (Fig. 4a) and the measured fluorescence lifetime <τ> *vs* $[K^+]_{out}$ data (Fig. 4b) to obtain a V_m *vs* <τ> relation (Fig. 4c). This relation is approximately piecewise linear, with a slope of 0.2 mV/ps (5 ps/mV) in the 850 ps – 1.2 ns range, and increasing to up to 0.8 mV/ps (1.2 ps/mV) for lower lifetimes (see Supplementary Note 8 for details). As shown in Fig. 4d, the calibration relation becomes increasingly uncertain as $[K^+]_{out}$ decreases, reflecting the saturation of VF2.1.Cl's quenching at very negative membrane potential in *B. subtilis*.

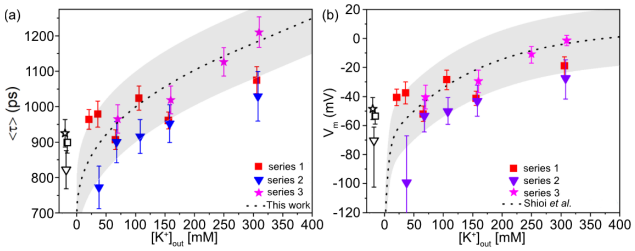

Figure 5: VF2.1.Cl lifetime measurements in *B. subtilis* cells in MSgg media exposed to variable external K^+ concentration in the presence of 25 µM valinomycin at constant medium osmolality ~770 mOsm/L. (a) Average lifetime and (b) estimated membrane potential using the calibration curve of Fig. 4c. The dashed curves correspond to the curves in Fig. 4b and 4d respectively, obtained at 650 mOsm/L external osmolality. The grayed areas correspond to these curves ± 100 ps and ± 20 mV respectively. Black symbols correspond respectively to the measured lifetimes and membrane potentials of *B. subtilis* in MSgg only (no valinomycin or added salts). It is noteworthy that the larger <τ> (resp. V_m) is in MSgg only, the larger it is in that series.

To assess the influence of osmolality (and therefore osmotic pressure) on these results, we performed similar measurements using a different total cation concentration equal to 300 mM (medium osmolality ~770 mOsm/L instead of 650 mOsm/L). The results, represented in (Fig. 5), are globally similar, with a day-to-day variability of about ±100 ps (Fig. 5a) equivalent to ±20 mV using the previous calibration (Fig. 5b). When adding increasing concentration of potassium without maintaining a constant osmolality, we observed a comparable increase of lifetime (or membrane

depolarization, see Supplementary Fig. 2) with increasing external K^+ concentration.

Altogether, these experiments suggest that in the presence of valinomycin, *B. subtilis*' membrane potential is determined mostly by the external potassium concentration, although some variations might be expected depending on the initial cell's physiological state (as discussed later).

To elucidate the possible role of potassium concentration, or more generally, of changing external conditions on the fluorescence of VF2.1.Cl itself, we measured its fluorescence decay in MSgg (in the absence of cells), and MSgg with valinomycin and with or without excess KCl. While addition of valinomycin (25 µM) only had negligible effect on VF2.1.Cl's lifetime ($\langle\tau\rangle_{MSgg,0}$ = 2.06 ns *vs* $\langle\tau\rangle_{MSgg,Val}$ = 2.22 ns), addition of excess of KCl (240-300 mM) in presence of valinomycin resulted in a noticeable decrease of VF2.1.Cl's lifetime ($\langle\tau\rangle_{MSgg,Val,KCl}$ = 1.74 ns, Supplementary Table 3 and Supplementary Fig. 3). Specifically, we observed that this variation was mainly due to changes in the respective fractions of the long and short decay components of the decay. The resulting decreased average lifetime ($\langle\tau\rangle_{MSgg,Val,KCl}$ = 1.74 ns) was still much larger than those recorded in the membrane of *B. subtilis* in all our measurements (0.75 ns < $\langle\tau\rangle_{mb}$ < 1.15 ns). This shows that, while VF2.1.Cl's lifetime in solution is surprisingly sensitive to its ionic environment, once inserted in the membrane of *B. subtilis*, the observed lifetime variations of VF2.1.Cl report on membrane potential changes (see Supplementary Note 9 for additional discussion).

As a control, valinomycin-treated *B. subtilis* cells were stained with VF2.0.Cl and subjected to the same external K^+ concentration changes. No significant variation in average lifetime $\langle\tau\rangle$ was observed in these experiments (Supplementary Fig. 4).

The previous measurements therefore demonstrate the potential of VF2.1.Cl as a fluorescence lifetime indicator for *B. subtilis*'s membrane potential. The fairly broad dispersion of lifetimes measured within cells exposed to a single condition

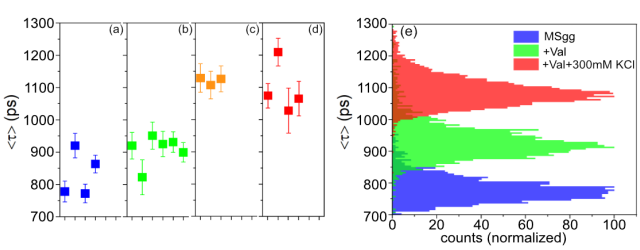

Figure 6: Average lifetime dispersion across measurements and external chemical conditions. Repeated measurements on different bacterial cultures resulted in slightly different measured average lifetimes in identical conditions. a: MSgg, b: MSgg + 25 µM valinomycin, c: same as (b) but with 240 mM KCl, d: same as (b) but with 300 mM KCl. e: In each measurement, the single-cell average lifetime was approximately normally distributed (with a few outliers not shown here), with standard deviation not fully accounted for by shot noise. Each histogram corresponds to the left-most datapoint with the same color in the left panel (the histogram for (c) is omitted as it overlaps with that of (d)). MSgg: $\langle\tau\rangle$ = 778 ± 32 ps, MSgg + Val: $\langle\tau\rangle$ = 920 ± 41 ps, MSgg + Val + 300 mM KCl: $\langle\tau\rangle$ = 1,075 ± 38 ps.

and between measurements of different populations in nominally identical conditions will be addressed next.

6. Single-cell membrane potential estimation of *B. subtilis* using V_m *vs* $\langle\tau\rangle$ calibration

We used the calibration curve obtained above to assess the membrane potential of *B. subtilis* cells in minimal medium (MSgg) in their unperturbed state based on the observed lifetimes (no valinomycin or added ions, Fig. 6a, blue squares and Supplementary Table 4). Focusing first on the *mean* observed values, we found $\langle\tau\rangle_{MSgg}$ = 835 ps on average (range: 772 – 920 ps), corresponding to a membrane potential $V_{m,MSgg}$ = -65 mV (range: -99 – -49 mV). The largest value is similar to that observed for *B. subtilis* cells in MSgg treated with 25 µM valinomycin (Fig. 6b, green squares): $V_{m,MSgg+Val}$ = -50 mV (range: -53 – -43 mV). The lowest is one of the smallest values we observed in all experiments performed with *B. subtilis* and for this reason is affected by the largest uncertainty (see Fig. 4c). It is however consistent with most values reported in the literature for the resting membrane potential of *B. subtilis* in minimal media.[2,28-30]

The broad range of measured lifetime in this "unperturbed" state might indicate that the assumption that cells prepared with our protocol and stained with VF2.1.Cl are "unperturbed" and reproducibly so, might be incorrect. In other words, minute variations in the preparation protocol might trigger physiological cell reactions resulting in different membrane potential measurements. This hypothesis would be consistent with the observation of ±20 mV or larger differences measured in different series of experiments in "identical" conditions (Fig. 5b). It is worth noting that these differences between measurements across series remain qualitatively similar as extracellular chemical conditions change from the "unperturbed" state to higher external salt concentration. A series with lower lifetime in MSgg (for instance Series 2 in Fig. 5a), will exhibit lower lifetimes throughout the series.

The lifetime variation from series to series remains approximately constant across different conditions (Fig. 6a-d), with mean lifetime dispersion in the "no perturbation" conditions of Fig. 6a-b being comparable to that observed in high $[K^+]_{out}$ measurements (Fig. 6c-d, orange and red squares). For these depolarized bacteria, we found $\langle\tau\rangle_{depol}$ = 1,105 ps on average across different measurements (range: 1,075 – 1,210 ps) which translates into an average membrane potential V_m^{depol} = -14 mV (range: -19 – -1 mV).

We turn next to the *dispersion* of measured lifetime values illustrated in representative histograms shown in Fig. 6e. The range of measured standard deviation $\sigma_{\langle\tau\rangle}$ is 24 - 70 ps across all measurements. While this may appear small, it represents 6 to 19% of the total range (760 – 1130 ps) of amplitude-averaged lifetimes recorded throughout our experiments. As discussed in Material & Methods and Supplementary Note 4, part of this dispersion can be attributed to the limited SNR of the FLIM data. Assuming uncorrelated contributions of shot noise and "other sources" to the observed lifetime variance, we can estimate the lifetime standard deviation due to these non-shot noise sources, $\sigma_{\langle\tau\rangle}^{Other}$, by:

$$\sigma_{\langle\tau\rangle}^{Other} = \sqrt{\left(\sigma_{\langle\tau\rangle}\right)^2 - \left(\sigma_{\langle\tau\rangle}^{SN}\right)^2} \qquad (5)$$

In all measurements, we find that shot noise accounts for only part of the observed amplitude-averaged lifetime dispersion (see Supplementary Table 5), with some measurements showing residual lifetime standard deviation up to ~60 ps, corresponding to ~12 mV using the approximate 0.2 mV/ps conversion coefficient of Fig. 4c. This additional dispersion is likely due to heterogeneity in the bacterial population, possibly related to difference in physiological states.

7. Probing the effect of medium osmolality on membrane potential

The calibration measurements (Fig. 4) and subsequent measurements performed at a different (constant) osmolality (Fig. 5) used small ions (Na^+, Cl^-) to maintain a constant osmolality. While potassium is the dominant species in the equilibration of the membrane potential in the presence of valinomycin, it cannot be excluded that using the Nernst potential equation for K^+ (Eq. (4)) instead of the Donnan equation (Eq. (3)) is leaving out some important details, especially at large external ion concentrations. In order to minimize these effects, we used xylose, a non-metabolizable and membrane-impermeable sugar to adjust the external medium's osmolality (Fig. 7, Table 1 and Supplementary Table 6).

Increasing the medium osmolality at constant $[K^+]_{out}$ should result in water expulsion from the cell in order to balance the osmotic pressure. Consequently, an increase of $[K^+]_{in}$ is expected, as has been well documented in *E. coli*.[81] This behavior, and the internalization of permeable solutes in the cytoplasm, is a general osmo-adaptation strategy of bacteria in response to physiological changes.[82] Assuming that water efflux dominates, this should be followed, according to the Nernst potential (Eq. (4)), by a decrease of the membrane potential. Similarly, increasing $[K^+]_{out}$ while keeping the medium osmolality constant should have little effect on $[K^+]_{in}$, and therefore, according to Eq. (4), should be followed by a membrane potential becoming less negative. Fig. 7 indicate these two types of changes by horizontal ($\Delta[K^+]_{out} = 0$, $\Delta Osm_{out} > 0$) or diagonal ($\Delta[K^+]_{out} > 0$, $\Delta Osm_{out} = 0$) arrows, their colors indicating agreement (green) or disagreement (red) with the above prediction of the Nernst potential. A third type of change is indicated by black vertical arrows in Fig. 7, corresponding to cases where $\Delta[K^+]_{out} > 0$ and $\Delta Osm > 0$, the increase in osmolality being mostly due to increasing $[K^+]_{out}$.

Table 1: *B. subtilis* membrane potential measurements in different external concentrations of KCl and xylose.

#	[Xyl] (mM)	$[KCl]_{out}$ (mM)	Osm_{out} (mOsm/L)	$V_m \pm \sigma$ (mV)
1	0	0	170	-50 ± 8
2	0	60	290	-34 ± 8
3	120	0	290	-125 +35/-17
4	120	60	410	-22 ± 10
5	180	60	470	-101 +25/-30
6	300	0	470	-54 ± 6
7	200	100	570	-29 ± 10
8	300	100	670	-59 +8/-11

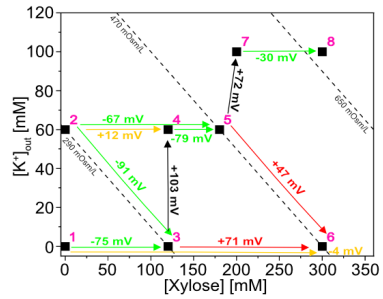

Figure 7: *B. subtilis* membrane potential measurements in different external concentrations of xylose and KCl in the presence of 25 μM of valinomycin. The black squares indicate the external xylose and KCl concentrations to which the cells were exposed. The measured V_m for the different measurements are tabulated in Table 1. Some of these conditions differ only by their $[K^+]_{out}$, while some others differ only by their osmolality (~[Xylose] + $2[K^+]_{out}$). The green and red arrows connect conditions between which either $\Delta[K^+]_{out} = 0$ and $\Delta Osm \neq 0$, or $\Delta Osm = 0$ and $\Delta[K^+]_{out} \neq 0$. The colors indicate agreement (green) or disagreement (red) with the sign of the membrane potential variation predicted by the Nernst potential (see Supplementary Table 6). The change in V_m is indicated next to each arrow. The orange arrows correspond to cases where almost no change in V_m is observed (within the typical measurement uncertainty of ± 20 mV), consistent with either a positive or negative change. The black arrows indicate changes where $\Delta[K^+]_{out} \neq 0$ and $\Delta Osm \neq 0$ but the sign of change cannot be predicted from the Nernst potential. Equi-osmolality lines are indicated by dashed diagonal lines.

Under these conditions, two opposing effects happen simultaneously, making the Nernst equation useless to predict the sign of the expected membrane potential change. Experimentally, our observations suggest that in conditions of large osmolality, the dominating effect is that of $\Delta[K^+]_{out} > 0$, associated with an increase of the membrane potential. The specificity of these stressful conditions could explain why our naïve use of the Nernst equation fails to predict the correct sign for the membrane potential change in this regime (red arrows in Fig. 7), in particular if K^+ influx is involved.[83,84]

8. Color-coded visualization of the membrane potential in *B. subtilis* cells

Although the calibration curve of Fig. 4c was obtained using the integrated signals of individual cells, it is formally possible to compute an amplitude-averaged lifetime for individual pixels of the image. Because of the lower SNR, the phasors of individual pixels are expected to exhibit a larger dispersion than those of individual cells, and correspondingly the single-pixel amplitude-averaged lifetimes are expected to be affected by a larger uncertainty than those of individual cells. Nonetheless the calibration curve of Fig. 4c can be used to convert single-pixel average lifetimes into membrane potential, which can then be color-coded and overlaid on the original image (Fig. 8). *B. subtilis* cells in minimal medium (MSgg) are characterized by a clearly larger negative membrane potential (Fig. 8a) than the cells expose to a high concentration of KCl in the presence of valinomycin (Fig. 8b), which exhibit a close to zero membrane potential, as expected from the loss of K^+ gradient across the membrane. These membrane potential maps enable visualizing not only the cell-to-cell variability observed in all single-cell results discussed in this work, but potentially as well, spatial

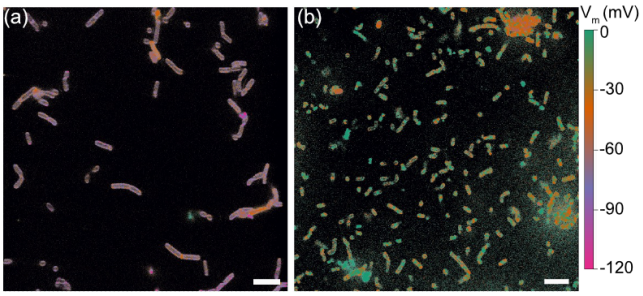

Figure 8. Effect of varying extracellular chemical conditions on the membrane potential of *B. subtilis*. (a) Unperturbed cells in MSgg only: V_m ~ -60 mV. (b) Chemically depolarized cells in MSgg (25 µM valinomycin + 240 mM KCl): V_m ~ -14 mV. For equivalent figures representing the average lifetime instead, see Supplementary Fig. 5. Scale bar = 10µm.

heterogeneity within individual cells, provided the single-pixel SNR is sufficient. This was not possible for these experiments, where a majority of pixels had counts of $N = 100$ photons or lower, resulting in an average lifetime uncertainty of ~146 ps or ~300 mV (see Supplementary Note 4 for details), too large to draw reliable conclusions at this point.

9. Conclusion & outlook

In conclusion, we have investigated the use of a novel kind of voltage-sensitive dye, VF2.1.Cl, previously used for membrane potential measurements in eukaryotic cells, for the study of the membrane potential of *B. subtilis*, a model for Gram-positive bacteria. In order to calibrate the fluorescence response of VF2.1.Cl to changes in the membrane potential of *B. subtilis*, we used a former study by Shioi *et al.* who measured change in internal K^+ in *B. subtilis* upon modulation of the external K^+ concentration. This approach allowed us to obtain a nonlinear relation between measured VF2.1.Cl fluorescence lifetime, obtained by phasor analysis of live cells FLIM data, and membrane potential.

Repeated measurements on cells exposed to series of increasing external concentration of K^+ ions indicated some variability of the measured lifetimes, which we tentatively attributed to variations in the cells physiological state at the time of harvesting prior to media perturbation, staining and imaging. These observed variations resulted in a ~ ±20 mV uncertainty in the reported membrane potential, which we showed to be unrelated to the measurement uncertainty due to shot noise and could be improved by a better control of the cell culture's initial state. Our measurements allowed interpreting most of the observed variations in VF2.1.Cl lifetime (and hence membrane potential) upon media (chemical composition) changes in a way that appeared for the most part consistent with the K^+ Nernst potential approximation for the membrane potential, and a simple interpretation of the effect of osmotic pressure change on the bacterial volume.

Our work raises a number of questions which further experiments will need to address.

The first question concerns the measured lifetimes of VF2.1.Cl in the membrane of *B. subtilis vs* those observed in eukaryotic cells. The range of lifetimes measured in *B. subtilis* cells with MP ranging from ~-100 mV to ~-10 mV was ~800 ps to 1.2 ns, significantly shorter than the lifetimes previously measured in eukaryotic cells (*e.g.* ~1.5 ns ≤ <τ> ≤ 2.1 ns in HEK293T cells with -80 mV < V_m < +80 mV [38]). This appears to be due in part to the different decay constants measured in these two systems. While Lazzarri *et al.* reported lifetime components τ_1 = 2.6 ns and τ_2 = 0.9 ns, we observed τ_1 in the [2.4, 3.2] ns range (median: 2.76 ns) and τ_2 in the [350, 740] ps range (median: 550 ps) depending on medium composition, which could explain the shorter average lifetimes observed in this work. Lazarri *et al.* reported a decrease in average lifetimes at high dye concentrations, but the dye concentration used in our work are in the low end of the range they explored, making dye concentration an unlikely explanation of these differences in lifetimes. On the other hand, the bacterial membrane as well as the ~34 nm thick external porous peptoglycan wall separating it from the external medium, [85] may provide a different chemical environment for VF2.1.Cl resulting in distinct photophysical characteristics. Moreover, bacterial cytoplasmic membranes are quite different from eukaryotic ones (lacking rigidifying sterols for instance), potentially contributing to these differences.[86,87] Alternatively, as mentioned in Supplementary Note 7, charge distribution within the bacterial wall may create a large enough electrical potential gradient outside of the bilayer to affect the effective potential drop across the membrane, which is what is sensed by the dye. [88]

The second and related question concern the voltage sensitivity of VF2.1.Cl in *B. subtilis*. In this work, we found that the average lifetime of VF2.1.Cl changes by ~5 ps/mV in the range -60 mV ≤ V_m ≤ 0 mV, its sensitivity dropping to ~1.2 ps/mV for more negative V_m values. This is different from the 3.5 ps/mV over the [-80, 80] mV range reported in HEK293T cells reported by Lazarri *et al.* Because this sensitivity is related, among other factors, to the respective orientation of the electric field and electric transition dipole of the molecule (supplementary Eq. S8) as well as their magnitude, this could indicate a different electric field magnitude in the bacterial membrane (due to a different membrane thickness, or as mentioned above, a contribution of the cell wall to the electric potential gradient), or a different average molecular orientation of VF2.1.Cl in the membrane.

Third, the facts that our calibration approach relies on past work that is difficult to reproduce,[2] and that we observed differences between measurements in presumably identical conditions (e.g. Fig. 5), hint at sources of variability that were not fully under control. Our work should thus be considered a first step towards establishing a robust V_m *vs* <τ> calibration for VF2.1.Cl in *B. subtilis*. One way to better control the cells' physiological state and minimize the delay between harvesting, medium replacement, staining and observation could involve studies performed in temperature-controlled microfluidic chambers, allowing rapid *in situ* medium exchange. A similar technology would also enable monitoring individual cell membrane potential evolution over time, whether isolated or within biofilms.

Alternatively, more direct ways of modulating the cell membrane potential such as induced transmembrane voltage application could be used, although it is unclear how reliably the actual applied field can be estimated based only on a geometric model of the bacterial shape. [26,27]

Notwithstanding, these open questions, which we plan to address in future work, our current results demonstrate the exciting potential of phasor-based, fluorescence lifetime measurement of VF dyes for precise and absolute potential measurements in bacterial cells. We anticipate that these and similar molecular indicators, together with advances in wide-field time-resolved detectors enabling simpler FLIM measurements[89,90], will enable new insights in the complex bioelectrical activity of bacterial communities.

10. Materials & Methods

Sample preparation for imaging: *B. subtilis* culture, growth and membrane staining protocols are described in Supplementary Note 1. Aliquots of *B. subtilis* cells were taken at the mid-log phase (during subculture) and were incubated with VF2.1.Cl for ~30 mins for staining. Stained bacterial cells were suspended in poly-L-lysine coated Petri dish with modified minimal salts glycerol glutamate (MSgg) medium, an optically transparent minimal medium (see Supplementary Table 1). Valinomycin, KCl, NaCl or xylose were added to the MSgg medium and the cells left incubating for at least 30 minutes before imaging.

Fluorescence lifetime imaging microscopy (FLIM): Several fields-of-view (FOV) of stained bacterial cells were imaged with a laser scanning confocal microscope equipped with time-correlated single-photon counting (TCSPC) hardware for fluorescence lifetime imaging microscopy (FLIM) (detailed in Supplementary Note 2).

Fluorescence lifetime information was analyzed using AlliGator, our freely available phasor- and NLSF FLIM analysis software, allowing cell-level or pixel-level fluorescence decay analysis.[62,66,91]

Fluorescence lifetime estimation by NLSF: In some cases, fluorescence lifetime estimation was done by nonlinear least-square fitting of the recorded photon arrival time histogram. The measured fluorescence decay can be expressed as [66]:

$$\begin{cases} S_T(t) = B + I_T \underset{T}{*} F_T(t) \\ F_T(t) = \sum_{i=1}^{2} A_i \exp\left(-\frac{(t-t_0)[T]}{\tau_i}\right) \end{cases} \quad (6)$$

where the notation introduced in ref. [65] are used, in which an index T indicate a T-periodic function (T being the laser period). The observed signal $S_T(t)$ is the convolution of the instrument response function (IRF) I_T with the fluorescence decay $F_T(t)$, modeled as a T-periodic bi-exponential function, plus a baseline parameter B accounting for residual uncorrelated background and an offset t_0. $t[T]$ denotes t modulo T. A_i and τ_i are the amplitude and lifetime of component i. where the amplitude A_i is related to signal intensity N_i (number of photocounts) by $N_i = A_i \tau_i$. The amplitude fractions are defined as $\alpha_i = A_i / (A_1 + A_2)$ from which the amplitude-averaged lifetime $\langle \tau \rangle_a$ is given by:

$$\langle \tau \rangle_a = \alpha_1 \tau_1 + \alpha_2 \tau_2 \quad (7)$$

while the intensity fractions are defined as $f_i = N_i / (N_1 + N_2)$. Parameters B, A_1, A_2, τ_1. and τ_2 are obtained using a standard iterative Levenberg-Marquard algorithm to minimize the (Poisson) weighted χ^2 function.[66]

Phasor analysis of fluorescence lifetime: Decays were converted into a calibrated phasor (g, s) as the normalized components of the first term of the decays' Fourier series as previously described,[62] using the IRF as calibration associated with lifetime $\tau = 0$ ns. Single pixel or single region of interest (ROI) phasors can be represented as a 2D histogram in the (g, s) plane. The phasor plot provides a user-friendly representation of complex decays due to its unique properties. Phasors corresponding to single exponential fluorescence decays are located on the so-called universal (semi)circle (UC) of radius 1/2 centered on (g, s) = (1/2, 1/2). In the case of a bi-exponential decay, the phasor is located on the segment connecting the two single-exponential decays' phasors (or "references"). References τ_1 and τ_2 were defined internally for each condition, by plotting a scatterplot of all cell-level phasors in that condition and finding the intersection of the major axis of inertia of the scatterplot with the universal circle (UC), location of single-exponential decays in the phasor representation (Figure 3b).

The relative distances of the phasor to these references (or phasor ratios, geometric quantities that are easily computed once the phasors are computed) correspond to the relative fractions f_i of each normalized single-exponential's phasor and are identical to the intensity-fractions of the single-exponential components of the decay.[92]

From these fractions, a mean lifetime can be computed as:[62]

$$\langle \tau \rangle_a = (f_1/\tau_1 + f_2/\tau_2)^{-1} \quad (8)$$

This phasor ratio-based average lifetime is formally identical to the amplitude-averaged lifetime defined by Eq. (7).[62] All mention of average lifetimes in the remainder of the text will refer to either one of these equivalent definitions of the amplitude-averaged lifetime, as it is the one relevant for the analysis of membrane potential with VoltageFluor dyes, as discussed in the next section. The index a (for amplitude-averaged) will also be dropped for simplicity.

A brief description of some of the phasor analysis steps follows, more details being provided in Supplementary Note 3.

Color-coded average lifetime map: In order to visualize individual bacterial cell MPs under different conditions, amplitude-averaged lifetime maps were computed from the pixel-wise phasor fractions using Eq. (8). A color scale was then used to encode amplitude-averaged lifetimes within a user-selected range, color which was then overlaid on the original image, the original pixel intensity (contrast-adjusted for clarity) being used to set the color brightness, as illustrated above in section 8.

Estimation of shot noise influence on the amplitude-averaged lifetime: In order to assess the relative contributions of population heterogeneity and signal-to-noise ratio (SNR) to the average lifetime distributions observed in our experiments, we performed Monte Carlo estimations of the influence of shot noise (the main noise contribution in the TCSPC

measurements performed here) to the computed single-cell average lifetime in the following manner. For each cell fluorescence decay $\{I(t_i)\}_{i=1,\ldots,G}$, we simulated $N = 1{,}000$ replicas of this decay, replacing each $I(t_i)$ by a random number $\mathrm{Poi}(I(t_i))$, and computing the corresponding $\langle\tau\rangle$ based on the same phasor references. The corresponding standard deviation $\sigma_{\langle\tau\rangle}^{SN}$ of the distribution of average lifetime is an estimation of the uncertainty on $\langle\tau\rangle$ computed for the single-cell decay due to shot noise, an approximation supported by direct simulation of shot noise-limited decays with identical photon counts (detailed in Supplementary Note 4).

ASSOCIATED CONTENT

Supporting Information

A Supplementary Information file containing additional figures, tables and notes is available free of charge on the ACS Publications website.

Data availability: Raw data files and analysis results will be freely available on Figshare by the time of publication.

Software availability: AlliGator is freely available on Github.[91]

AUTHOR INFORMATION

Corresponding Authors: XM & SW

Shimon Weiss − *UCLA-DOE Institute for Genomics and Proteomics, Department of Biological Chemistry, University of California at Los Angeles, Los Angeles, CA 90095, USA; Department of Chemistry and Biochemistry, University of California at Los Angeles, Los Angeles, CA 90095, USA; Department of Physiology, University of California at Los Angeles, Los Angeles, CA 90095, USA; California Nano Systems Institute, University of California at Los Angeles, Los Angeles, CA 90095, USA; Department of Physics, Institute for Nanotechnology and Advanced Materials, Bar-Ilan University, Ramat-Gan 52900, Israel; http://orcid.org/0000-0002-0720-5426*

Email: sweiss@chem.ucla.edu

Xavier Michalet − *[2]Department of Chemistry and Biochemistry, University of California at Los Angeles, Los Angeles, CA 90095, USA; [5]California Nano Systems Institute, University of California at Los Angeles, Los Angeles, CA 90095, USA; https://orcid.org/0000-0001-6602-7693*

Email: michalet@chem.ucla.edu

Author Contributions

DR, XM & SW designed the experiments. DR performed experiments and conducted data analysis. XM wrote the software, theory and contributed data analysis concepts. EM provided the VFs. DR and XM wrote the manuscript, which was edited by all other authors. All authors have given approval to the final version of the manuscript.

Funding Sources

This research is supported by funding from Office of Biological & Environmental Research Program (BER) of the Department of Energy Office of Science, grant DE-SC0020338 and DE-SC0023184; and NIH grant R35GM153237.

Notes

The authors declare no competing financial interest.

ACKNOWLEDGMENT

The authors would like to thank Dr. Kiran Bharadwaj for her continuous support and feedback throughout the research process.

REFERENCES

(1) Miller, E. W. Small molecule fluorescent voltage indicators for studying membrane potential. *Current Opinion in Chemical Biology* **2016**, *33*, 74-80. DOI: 10.1016/j.cbpa.2016.06.003.

(2) Shioi, J. I.; Matsuura, S.; Imae, Y. Quantitative measurements of proton motive force and motility in Bacillus subtilis. *Journal of Bacteriology* **1980**, *144* (3), 891-897. DOI: 10.1128/jb.144.3.891-897.1980.

(3) Levin, M. Molecular bioelectricity: how endogenous voltage potentials control cell behavior and instruct pattern regulation in vivo. *Mol Biol Cell* **2014**, *25* (24), 3835-3850. DOI: 10.1091/mbc.E13-12-0708.

(4) Benarroch, J. M.; Asally, M. The Microbiologist's Guide to Membrane Potential Dynamics. *Trends Microbiol* **2020**, *28* (4), 304-314. DOI: 10.1016/j.tim.2019.12.008.

(5) Abdul Kadir, L.; Stacey, M.; Barrett-Jolley, R. Emerging Roles of the Membrane Potential: Action Beyond the Action Potential. *Frontiers in Physiology* **2018**, *9*. DOI: 10.3389/fphys.2018.01661.

(6) Jones, J. M.; Larkin, J. W. Toward Bacterial Bioelectric Signal Transduction. *Bioelectricity* **2021**, *3* (2), 116-119. DOI: 10.1089/bioe.2021.0013.

(7) Dimroth, P.; Kaim, G.; Matthey, U. Crucial Role of the Membrane Potential for ATP Synthesis by F1Fo ATP Synthases. *Journal of Experimental Biology* **2000**, *203* (1), 51-59. DOI: 10.1242/jeb.203.1.51.

(8) Poole, R. J. Energy Coupling for Membrane Transport. *Annual Review of Plant Physiology* **1978**, *29* (1), 437-460. DOI: 10.1146/annurev.pp.29.060178.002253.

(9) Strahl, H.; Hamoen, L. W. Membrane potential is important for bacterial cell division. *Proceedings of the National Academy of Sciences* **2010**, *107* (27), 12281-12286. DOI: 10.1073/pnas.1005485107.

(10) Martinez-Corral, R.; Liu, J.; Prindle, A.; Suel, G. M.; Garcia-Ojalvo, J. Metabolic basis of brain-like electrical signalling in bacterial communities. *Philos Trans R Soc Lond B Biol Sci* **2019**, *374* (1774), 20180382. DOI: 10.1098/rstb.2018.0382.

(11) Wood, J. M. Osmosensing by Bacteria: Signals and Membrane-Based Sensors. *Microbiology and Molecular Biology Reviews* **1999**, *63* (1), 230-262. DOI: 10.1128/mmbr.63.1.230-262.1999.

(12) Bruni, G. N.; Weekley, R. A.; Dodd, B. J. T.; Kralj, J. M. Voltage-gated calcium flux mediates Escherichia coli mechanosensation. *Proc Natl Acad Sci U S A* **2017**, *114* (35), 9445-9450. DOI: 10.1073/pnas.1703084114.

(13) Miller, J. B.; Koshland, D. E. Sensory electrophysiology of bacteria: relationship of the membrane potential to motility and chemotaxis in Bacillus subtilis. *Proceedings of*

the National Academy of Sciences **1977**, *74* (11), 4752-4756. DOI: 10.1073/pnas.74.11.4752.
(14) Damper, P. D.; Epstein, W. Role of the membrane potential in bacterial resistance to aminoglycoside antibiotics. *Antimicrobial Agents and Chemotherapy* **1981**, *20* (6), 803-808. DOI: 10.1128/aac.20.6.803.
(15) Prindle, A.; Liu, J.; Asally, M.; Ly, S.; Garcia-Ojalvo, J.; Suel, G. M. Ion channels enable electrical communication in bacterial communities. *Nature* **2015**, *527* (7576), 59-63. DOI: 10.1038/nature15709.
(16) Liu, J.; Martinez-Corral, R.; Prindle, A.; Lee, D. D.; Larkin, J.; Gabalda-Sagarra, M.; Garcia-Ojalvo, J.; Suel, G. M. Coupling between distant biofilms and emergence of nutrient time-sharing. *Science* **2017**, *356* (6338), 638-642. DOI: 10.1126/science.aah4204.
(17) Kikuchi, K.; Galera-Laporta, L.; Weatherwax, C.; Lam, J. Y.; Moon, E. C.; Theodorakis, E. A.; Garcia-Ojalvo, J.; Süel, G. M. Electrochemical potential enables dormant spores to integrate environmental signals. *Science* **2022**, *378* (6615), 43-49. DOI: doi:10.1126/science.abl7484.
(18) Hamill, O. P.; Marty, A.; Neher, E.; Sakmann, B.; Sigworth, F. J. Improved patch-clamp techniques for high-resolution current recording from cells and cell-free membrane patches. *Pflügers Archiv - European Journal of Physiology* **1981**, *391* (2), 85-100. DOI: 10.1007/bf00656997.
(19) Sakmann, B.; Neher, E. *Single-Channel Recording*; 1995. DOI: 10.1007/978-1-4419-1229-9.
(20) Buzsáki, G. Large-scale recording of neuronal ensembles. *Nature Neuroscience* **2004**, *7* (5), 446-451. DOI: 10.1038/nn1233.
(21) Jun, J. J.; Steinmetz, N. A.; Siegle, J. H.; Denman, D. J.; Bauza, M.; Barbarits, B.; Lee, A. K.; Anastassiou, C. A.; Andrei, A.; Aydın, Ç.; et al. Fully integrated silicon probes for high-density recording of neural activity. *Nature* **2017**, *551* (7679), 232-236. DOI: 10.1038/nature24636.
(22) Obien, M. E. J.; Deligkaris, K.; Bullmann, T.; Bakkum, D. J.; Frey, U. Revealing neuronal function through microelectrode array recordings. *Frontiers in Neuroscience* **2015**, *8*. DOI: 10.3389/fnins.2014.00423.
(23) Felle, H.; Porter, J. S.; Slayman, C. L.; Kaback, H. R. Quantitative measurements of membrane potential in Escherichia coli. *Biochemistry* **1980**, *19* (15), 3585-3590. DOI: 10.1021/bi00556a026 From NLM Medline.
(24) Ehrenberg, B.; Montana, V.; Wei, M. D.; Wuskell, J. P.; Loew, L. M. Membrane potential can be determined in individual cells from the nernstian distribution of cationic dyes. *Biophys J* **1988**, *53* (5), 785-794. DOI: 10.1016/s0006-3495(88)83158-8 From NLM.
(25) Mancini, L.; Terradot, G.; Tian, T.; Pu, Y.; Li, Y.; Lo, C. J.; Bai, F.; Pilizota, T. A General Workflow for Characterization of Nernstian Dyes and Their Effects on Bacterial Physiology. *Biophys J* **2020**, *118* (1), 4-14. DOI: 10.1016/j.bpj.2019.10.030.
(26) Kralj, J. M.; Hochbaum, D. R.; Douglass, A. D.; Cohen, A. E. Electrical spiking in Escherichia coli probed with a fluorescent voltage-indicating protein. *Science* **2011**, *333* (6040), 345-348. DOI: 10.1126/science.1204763.
(27) Stratford, J. P.; Edwards, C. L. A.; Ghanshyam, M. J.; Malyshev, D.; Delise, M. A.; Hayashi, Y.; Asally, M. Electrically induced bacterial membrane-potential dynamics correspond to cellular proliferation capacity. *Proc Natl Acad Sci U S A* **2019**, *116* (19), 9552-9557. DOI: 10.1073/pnas.1901788116.
(28) Hosoi, S.; Mochizuki, N.; Hayashi, S.; Kasai, M. Control of membrane potential by external H+ concentration in Bacillus subtilis as determined by an ion-selective electrode. *Biochim Biophys Acta* **1980**, *600* (3), 844-852. DOI: 10.1016/0005-2736(80)90487-3 From NLM Medline.
(29) Zaritsky, A.; Kihara, M.; Macnab, R. M. Measurement of membrane potential in Bacillus subtilis: a comparison of lipophilic cations, rubidium ion, and a cyanine dye as probes. *J Membr Biol* **1981**, *63* (3), 215-231. DOI: 10.1007/BF01870983 From NLM Medline.
(30) Te Winkel, J. D.; Gray, D. A.; Seistrup, K. H.; Hamoen, L. W.; Strahl, H. Analysis of Antimicrobial-Triggered Membrane Depolarization Using Voltage Sensitive Dyes. *Front Cell Dev Biol* **2016**, *4*, 29. DOI: 10.3389/fcell.2016.00029 From NLM PubMed-not-MEDLINE.
(31) Pirbadian, S.; Chavez, M. S.; El-Naggar, M. Y. Spatiotemporal mapping of bacterial membrane potential responses to extracellular electron transfer. *Proceedings of the National Academy of Sciences* **2020**, *117* (33), 20171-20179. DOI: 10.1073/pnas.2000802117.
(32) Mancini, L.; Terradot, G.; Tian, T.; Pu, Y.; Li, Y.; Lo, C.-J.; Bai, F.; Pilizota, T. A General Workflow for Characterization of Nernstian Dyes and Their Effects on Bacterial Physiology. *Biophysical Journal* **2020**, *118* (1), 4-14. DOI: 10.1016/j.bpj.2019.10.030.
(33) Effect of Thioflavin T on the Elongation Rate of Bacteria. *Bioelectricity* **2022**, *4* (1), 12-17. DOI: 10.1089/bioe.2021.0027.
(34) Brinks, D.; Klein, A. J.; Cohen, A. E. Two-Photon Lifetime Imaging of Voltage Indicating Proteins as a Probe of Absolute Membrane Voltage. *Biophys J* **2015**, *109* (5), 914-921. DOI: 10.1016/j.bpj.2015.07.038.
(35) Bando, Y.; Sakamoto, M.; Kim, S.; Ayzenshtat, I.; Yuste, R. Comparative Evaluation of Genetically Encoded Voltage Indicators. *Cell Reports* **2019**, *26* (3), 802-813.e804. DOI: 10.1016/j.celrep.2018.12.088.
(36) Miller, E. W.; Lin, J. Y.; Frady, E. P.; Steinbach, P. A.; Kristan, W. B., Jr.; Tsien, R. Y. Optically monitoring voltage in neurons by photo-induced electron transfer through molecular wires. *Proc Natl Acad Sci U S A* **2012**, *109* (6), 2114-2119. DOI: 10.1073/pnas.1120694109 From NLM Medline.
(37) Woodford, C. R.; Frady, E. P.; Smith, R. S.; Morey, B.; Canzi, G.; Palida, S. F.; Araneda, R. C.; Kristan, W. B.; Kubiak, C. P.; Miller, E. W.; et al. Improved PeT Molecules for Optically Sensing Voltage in Neurons. *Journal of the American Chemical Society* **2015**, *137* (5), 1817-1824. DOI: 10.1021/ja510602z.
(38) Lazzari-Dean, J. R.; Gest, A. M.; Miller, E. W. Optical estimation of absolute membrane potential using fluorescence lifetime imaging. *Elife* **2019**, *8*. DOI: 10.7554/eLife.44522.
(39) Lazzari-Dean, J. R.; Gest, A. M. M.; Miller, E. W. Measuring Absolute Membrane Potential Across Space and Time. *Annual Review of Biophysics* **2021**, *50* (1), 447-468. DOI: 10.1146/annurev-biophys-062920-063555.
(40) Lakowicz, J. R. *Principles of Fluorescence Spectroscopy*; 2006. DOI: 10.1007/978-0-387-46312-4.

(41) Suhling, K.; Hirvonen, L. M.; Levitt, J. A.; Chung, P.-H.; Tregidgo, C.; Le Marois, A.; Rusakov, D. A.; Zheng, K.; Ameer-Beg, S.; Poland, S.; et al. Fluorescence lifetime imaging (FLIM): Basic concepts and some recent developments. *Medical Photonics* **2015**, *27*, 3-40. DOI: 10.1016/j.medpho.2014.12.001.
(42) Datta, R.; Heaster, T. M.; Sharick, J. T.; Gillette, A. A.; Skala, M. C. Fluorescence lifetime imaging microscopy: fundamentals and advances in instrumentation, analysis, and applications. *Journal of Biomedical Optics* **2020**, *25* (07). DOI: 10.1117/1.Jbo.25.7.071203.
(43) Oleksiievets, N.; Mathew, C.; Thiele, J. C.; Gallea, J. I.; Nevskyi, O.; Gregor, I.; Weber, A.; Tsukanov, R.; Enderlein, J. Single-Molecule Fluorescence Lifetime Imaging Using Wide-Field and Confocal-Laser Scanning Microscopy: A Comparative Analysis. *Nano Letters* **2022**, *22* (15), 6454-6461. DOI: 10.1021/acs.nanolett.2c01586.
(44) Li, L.-s. Fluorescence Probes for Membrane Potentials Based on Mesoscopic Electron Transfer. *Nano Letters* **2007**, *7* (10), 2981-2986. DOI: 10.1021/nl071163p.
(45) Kulkarni, R. U.; Yin, H.; Pourmandi, N.; James, F.; Adil, M. M.; Schaffer, D. V.; Wang, Y.; Miller, E. W. A Rationally Designed, General Strategy for Membrane Orientation of Photoinduced Electron Transfer-Based Voltage-Sensitive Dyes. *ACS Chem Biol* **2017**, *12* (2), 407-413. DOI: 10.1021/acschembio.6b00981.
(46) de Silva, A. P.; Gunaratne, H. Q. N.; Habib-Jiwan, J. L.; McCoy, C. P.; Rice, T. E.; Soumillion, J. P. New Fluorescent Model Compounds for the Study of Photoinduced Electron Transfer: The Influence of a Molecular Electric Field in the Excited State. *Angewandte Chemie International Edition in English* **1995**, *34* (16), 1728-1731. DOI: 10.1002/anie.199517281.
(47) Boggess, S. C.; Lazzari-Dean, J. R.; Raliski, B. K.; Mun, D. M.; Li, A. Y.; Turnbull, J. L.; Miller, E. W. Fluorescence lifetime predicts performance of voltage sensitive fluorophores in cardiomyocytes and neurons. *RSC Chem Biol* **2021**, *2* (1), 248-258. DOI: 10.1039/d0cb00152j.
(48) Liu, P.; Miller, E. W. Electrophysiology, Unplugged: Imaging Membrane Potential with Fluorescent Indicators. *Acc Chem Res* **2020**, *53* (1), 11-19. DOI: 10.1021/acs.accounts.9b00514.
(49) Gest, A. M. M.; Yaeger-Weiss, S. K.; Lazzari-Dean, J. R.; Miller, E. W. VoltageFluor dyes and fluorescence lifetime imaging for optical measurement of membrane potential. In *Ion Channels: Channel Production and Optical Methods*, Methods in Enzymology, 2021; pp 267-293.
(50) Lazzari-Dean, J. R.; Miller, E. W. Optical Estimation of Absolute Membrane Potential Using One- and Two-Photon Fluorescence Lifetime Imaging Microscopy. *Bioelectricity* **2021**, *3* (3), 197-203. DOI: 10.1089/bioe.2021.0007.
(51) Gest, A. M. M.; Lazzari-Dean, J. R.; Ortiz, G.; Yaeger-Weiss, S. K.; Boggess, S. C.; Miller, E. W. **2023**. DOI: 10.1101/2023.10.06.561080.
(52) Pelet, S.; Previte, M. J. R.; Laiho, L. H.; So, P. T. C. A Fast Global Fitting Algorithm for Fluorescence Lifetime Imaging Microscopy Based on Image Segmentation. *Biophysical Journal* **2004**, *87* (4), 2807-2817. DOI: 10.1529/biophysj.104.045492.
(53) Periasamy, N. Analysis of Fluorescence Decay by the Nonlinear Least Squares Method. *Biophysical Journal* **1988**, *54* (5), 961-967. DOI: 10.1016/s0006-3495(88)83032-7.
(54) Jameson, D. M.; Gratton, E.; Hall, R. D. The Measurement and Analysis of Heterogeneous Emissions by Multifrequency Phase and Modulation Fluorometry. *Applied Spectroscopy Reviews* **2007**, *20* (1), 55-106. DOI: 10.1080/05704928408081716.
(55) Digman, M. A.; Caiolfa, V. R.; Zamai, M.; Gratton, E. The Phasor Approach to Fluorescence Lifetime Imaging Analysis. *Biophysical Journal* **2008**, *94* (2), L14-L16. DOI: 10.1529/biophysj.107.120154.
(56) Ranjit, S.; Malacrida, L.; Jameson, D. M.; Gratton, E. Fit-free analysis of fluorescence lifetime imaging data using the phasor approach. *Nature Protocols* **2018**, *13* (9), 1979-2004. DOI: 10.1038/s41596-018-0026-5.
(57) Vallmitjana, A.; Dvornikov, A.; Torrado, B.; Jameson, D. M.; Ranjit, S.; Gratton, E. Resolution of 4 components in the same pixel in FLIM images using the phasor approach. *Methods and Applications in Fluorescence* **2020**, *8* (3). DOI: 10.1088/2050-6120/ab8570.
(58) Redford, G. I.; Clegg, R. M. Polar Plot Representation for Frequency-Domain Analysis of Fluorescence Lifetimes. *Journal of Fluorescence* **2005**, *15* (5), 805-815. DOI: 10.1007/s10895-005-2990-8.
(59) Clayton, A. H. A.; Hanley, Q. S.; Verveer, P. J. Graphical representation and multicomponent analysis of single-frequency fluorescence lifetime imaging microscopy data. *Journal of Microscopy* **2004**, *213* (1), 1-5. DOI: 10.1111/j.1365-2818.2004.01265.x.
(60) Colyer, R. A.; Siegmund, O. H. W.; Tremsin, A. S.; Vallerga, J. V.; Weiss, S.; Michalet, X. Phasor imaging with a widefield photon-counting detector. *Journal of Biomedical Optics* **2012**, *17* (1). DOI: 10.1117/1.Jbo.17.1.016008.
(61) Burri, S.; Maruyama, Y.; Michalet, X.; Regazzoni, F.; Bruschini, C.; Charbon, E. Architecture and applications of a high resolution gated SPAD image sensor. *Opt Express* **2014**, *22* (14), 17573-17589. DOI: 10.1364/OE.22.017573.
(62) Chen, S. J.; Sinsuebphon, N.; Rudkouskaya, A.; Barroso, M.; Intes, X.; Michalet, X. In vitro and in vivo phasor analysis of stoichiometry and pharmacokinetics using short-lifetime near-infrared dyes and time-gated imaging. *Journal of Biophotonics* **2018**, *12* (3). DOI: 10.1002/jbio.201800185.
(63) Ulku, A. C.; Bruschini, C.; Antolovic, I. M.; Charbon, E.; Kuo, Y.; Ankri, R.; Weiss, S.; Michalet, X. A 512x512 SPAD Image Sensor with Integrated Gating for Widefield FLIM. *IEEE J Sel Top Quantum Electron* **2019**, *25* (1). DOI: 10.1109/JSTQE.2018.2867439.
(64) Ulku, A.; Ardelean, A.; Antolovic, M.; Weiss, S.; Charbon, E.; Bruschini, C.; Michalet, X. Wide-field time-gated SPAD imager for phasor-based FLIM applications. *Methods and Applications in Fluorescence* **2020**, *8* (2). DOI: 10.1088/2050-6120/ab6ed7.
(65) Michalet, X. Continuous and discrete phasor analysis of binned or time-gated periodic decays. *AIP Advances* **2021**, *11* (3). DOI: 10.1063/5.0027834.
(66) Smith, J. T.; Rudkouskaya, A.; Gao, S.; Gupta, J. M.; Ulku, A.; Bruschini, C.; Charbon, E.; Weiss, S.; Barroso, M.; Intes, X.; et al. In vitro and in vivo NIR fluorescence lifetime imaging with a time-gated SPAD camera. *Optica* **2022**, *9* (5). DOI: 10.1364/optica.454790.
(67) Scherer, P. O. J.; Fischer, S. F. *Theoretical Molecular Biophysics*; Springer, 2017. DOI: 10.1007/978-3-662-55671-9.

(68) Walz, D.; Bamberg, E.; Lauger, P. Nonlinear Electrical Effects in Lipid Bilayer Membranes .I. Ion Injection. *Biophysical Journal* **1969**, *9* (9), 1150-&. DOI: 10.1016/S0006-3495(69)86442-8.
(69) Everitt, C. T.; Haydon, D. A. Electrical Capacitance of a Lipid Membrane Separating 2 Aqueous Phases. *Journal of Theoretical Biology* **1968**, *18* (3), 371-&. DOI: 10.1016/0022-5193(68)90084-2.
(70) Lauger, P.; Lesslauer, W.; Marti, E.; Richter, J. Electrical Properties of Bimolecular Phospholipid Membranes. *Biochimica Biophysica Acta* **1967**, *135* (1), 20-+. DOI: 10.1016/0005-2736(67)90004-1.
(71) Donnan, F. G. Theory of membrane equilibria and membrane potentials in the presence of non-dialysing electrolytes. A contribution to physical-chemical physiology. *Journal of Membrane Science* **1995**, *100* (1), 45-55. DOI: 10.1016/0376-7388(94)00297-c.
(72) Pressman, B. C. Biological applications of ionophores. *Annu Rev Biochem* **1976**, *45*, 501-530. DOI: 10.1146/annurev.bi.45.070176.002441 From NLM Medline.
(73) Kaushik, V.; Yakisich, J. S.; Kumar, A.; Azad, N.; Iyer, A. K. V. Ionophores: Potential Use as Anticancer Drugs and Chemosensitizers. *Cancers (Basel)* **2018**, *10* (10). DOI: 10.3390/cancers10100360 From NLM PubMed-not-MEDLINE.
(74) Novilla, M. N.; McClary, D.; Laudert, S. B. Chapter 29 - Ionophores. In *Reproductive and Developmental Toxicology (Second Edition)*, Gupta, R. C. Ed.; Academic Press, 2017; pp 503-518.
(75) Mueller, P.; Rudin, D. O. Development of K+-Na+ discrimination in experimental bimolecular lipid membranes by macrocyclic antibiotics. *Biochem Biophys Res Commun* **1967**, *26* (4), 398-404. DOI: 10.1016/0006-291x(67)90559-1 From NLM Medline.
(76) Freedman, J. C. Chapter 4 – Ionophores in Planar Lipid Bilayers. 2011.
(77) Su, Z.; Ran, X.; Leitch, J. J.; Schwan, A. L.; Faragher, R.; Lipkowski, J. How Valinomycin Ionophores Enter and Transport K(+) across Model Lipid Bilayer Membranes. *Langmuir* **2019**, *35* (51), 16935-16943. DOI: 10.1021/acs.langmuir.9b03064 From NLM Medline.
(78) Huang, S.; Liu, Y.; Liu, W. Q.; Neubauer, P.; Li, J. The Nonribosomal Peptide Valinomycin: From Discovery to Bioactivity and Biosynthesis. *Microorganisms* **2021**, *9* (4). DOI: 10.3390/microorganisms9040780 From NLM PubMed-not-MEDLINE.
(79) Inai, Y.; Yabuki, M.; Kanno, T.; Akiyama, J.; Yasuda, T.; Utsumi, K. Valinomycin induces apoptosis of ascites hepatoma cells (AH-130) in relation to mitochondrial membrane potential. *Cell Struct Funct* **1997**, *22* (5), 555-563. DOI: 10.1247/csf.22.555 From NLM Medline.
(80) Shapiro, H. M. Cell membrane potential analysis. *Methods Cell Biol* **1994**, *41*, 121-133. DOI: 10.1016/s0091-679x(08)61713-6 From NLM Medline.
(81) Epstein, W.; Schultz, S. G. Cation Transport in Escherichia coli. *The Journal of General Physiology* **1965**, *49* (2), 221-234. DOI: 10.1085/jgp.49.2.221.
(82) Sleator, R. D.; Hill, C. Bacterial osmoadaptation: the role of osmolytes in bacterial stress and virulence. *FEMS Microbiology Reviews* **2002**, *26* (1), 49-71. DOI: 10.1111/j.1574-6976.2002.tb00598.x.
(83) Whatmore, A. M.; Chudek, J. A.; Reed, R. H. The effects of osmotic upshock on the intracellular solute pools of Bacillus subtilis. *Journal of General Microbiology* **1990**, *136* (12), 2527-2535. DOI: 10.1099/00221287-136-12-2527.
(84) Whatmore, A. M.; Reed, R. H. Determination of turgor pressure in Bacillus subtilis: a possible role for K+ in turgor regulation. *Journal of General Microbiology* **1990**, *136* (12), 2521-2526. DOI: 10.1099/00221287-136-12-2521.
(85) Pasquina-Lemonche, L.; Burns, J.; Turner, R. D.; Kumar, S.; Tank, R.; Mullin, N.; Wilson, J. S.; Chakrabarti, B.; Bullough, P. A.; Foster, S. J.; et al. The architecture of the Gram-positive bacterial cell wall. *Nature* **2020**, *582* (7811), 294-297. DOI: 10.1038/s41586-020-2236-6.
(86) Strahl, H.; Errington, J. Bacterial Membranes: Structure, Domains, and Function. *Annual Review of Microbiology* **2017**, *71* (1), 519-538. DOI: 10.1146/annurev-micro-102215-095630.
(87) Kaiser, H.-J.; Surma, M. A.; Mayer, F.; Levental, I.; Grzybek, M.; Klemm, R. W.; Da Cruz, S.; Meisinger, C.; Müller, V.; Simons, K.; et al. Molecular Convergence of Bacterial and Eukaryotic Surface Order. *Journal of Biological Chemistry* **2011**, *286* (47), 40631-40637. DOI: 10.1074/jbc.M111.276444.
(88) Barbosa, N. S. V.; Lima, E. R. A.; Tavares, F. W. The electrostatic behavior of the bacterial cell wall using a smoothing function to describe the charge-regulated volume charge density profile. *Colloids and Surfaces B: Biointerfaces* **2015**, *134*, 447-452. DOI: 10.1016/j.colsurfb.2015.06.066.
(89) Bruschini, C.; Homulle, H.; Antolovic, I. M.; Burri, S.; Charbon, E. Single-photon avalanche diode imagers in biophotonics: review and outlook. *Light: Science & Applications* **2019**, *8* (1). DOI: 10.1038/s41377-019-0191-5.
(90) Ulku, A.; Ardelean, A.; Antolovic, M.; Weiss, S.; Charbon, E.; Bruschini, C.; Michalet, X. Wide-field time-gated SPAD imager for phasor-based FLIM applications. *Methods and Applications in Fluorescence* **2020**, *8* (2), 024002. DOI: 10.1088/2050-6120/ab6ed7.
(91) *AlliGator software*; UCLA: Github, 2024. https://github.com/smXplorer/AlliGator.
(92) Chen, S. J.; Sinsuebphon, N.; Rudkouskaya, A.; Barroso, M.; Intes, X.; Michalet, X. In vitro and in vivo phasor analysis of stoichiometry and pharmacokinetics using short-lifetime near-infrared dyes and time-gated imaging. *Journal of Biophotonics* **2018**, *12* (3), e201800185. DOI: 10.1002/jbio.201800185.